

# Chapter 1

## Observations

AU Mic was observed with ALMA on three dates: 26 March 2014, 18 August 2014, and 24 June 2015. All observations were configured with four spectral windows, and employed ALMA’s 12m antennas and Band 7 receivers. One spectral window was centered around the CO  $J = (2 - 1)$  transition at a frequency of 230.538001 GHz, with a total bandwidth of 1.875 GHz and a channel spacing of 0.6 km/s. The remaining three spectral windows were configured to detect continuum emission with central frequencies of 228.5, 213.5, and 216.0 GHz, total bandwidths of 2 GHz, and channel spacings of 21.7 km/s.

Information regarding the three observation dates can be found in Table 1.1. The short-baseline March observation provides information about AU Mic’s disk on large spatial scales; in contrast, the subsequent long-baseline August observation was intended to trace the small-scale structure of the disk. The quality of the gain transfer for the August observation was tested using observations of the quasar J2057-3734.

**Table 1.1:** Observation Information

	26 March 2014	18 August 2014	24 June 2015
Antennas:	32	35	37
Baseline length (m):	14–437	20–1268	30–1431
On-source time (min):	35	35	33
Flux calibrator:	Titan	J2056-472	Titan
Bandpass calibrator:	J1924-2914	J2056-4714	J1924-2914
Phase calibrator:	J2101-2933	J2101-2933	J2056-3208
pwv (mm):	0.6	1.6	0.7

The long-baseline August data were supplemented with a second night of higher-quality observations (as indicated by the relative pwv levels) in June 2015. The quasar J2101-2933 was used to assess the gain transfer quality. During the last segment of the June observation (04:23:38–04:29:58 UT), the host star flared.

Calibration, reduction, and imaging were carried out using the **CASA** and **MIRIAD** software packages. Standard ALMA reduction scripts were applied to the datasets: phase calibration was accomplished via water vapor radiometry tables, and system temperature calibrations were performed to account for variations in instrument and weather conditions. Flux and bandpass calibrations were subsequently applied.

To determine the flux of the flare as a function of time, we binned the data into one-minute intervals using the **CASA** task `split` and fit a point source in each bin to baselines between 100 k $\lambda$  and 1400 k $\lambda$  with `uvmodelfit`. The resulting flare fits can be found in Table 1.2. We exclude from our analysis the seven minutes during which the flare occurred, as it proved difficult to separate the stellar emission from the disk emission while it was changing so rapidly.

AU Mic’s equatorial coordinates were not well constrained across our observations

**Table 1.2:** Subtracted point-source fluxes

Time (UTC)	Point-source Flux ( $\mu\text{Jy}$ )
03:45:0–04:20:0 (no flare)	$(4.1 \pm 0.2) \times 10^2$
4:23:38–4:24:00	$(9.2 \pm 1.7) \times 10^2$
4:24:00–4:25:00	$(1.146 \pm 0.010) \times 10^4$
4:25:00–4:26:00	$(3.59 \pm 0.10) \times 10^3$
4:26:00–4:27:00	$(1.58 \pm 0.10) \times 10^3$
4:27:00–4:28:00	$(4.50 \pm 1.0) \times 10^2$
4:28:00–4:29:00	$(4.60 \pm 1.0) \times 10^2$
4:29:00–4:29:58	$(5.20 \pm 1.0) \times 10^2$

due to the star’s high proper motion. We fit an image-domain elliptical gaussian to a small region around the star on each date with the task `imfit`, and used the centroid of the Gaussian fit to define the star position. We note that for the June data, the exclusion of the flare changed the centroid of the Gaussian fit by  $0.07''$ , i.e.  $\sim 2$  pixels. This could be explained if the flare were not symmetric with respect to the star. Finally, each dataset was phase shifted using the task `fixvis` so that the pointing center of the data was the same as the fitted star position.

Imaging was performed using standard Fourier inversion methods as implemented in the **CASA** task `tclean`. Two weighting schemes were used: (i) natural weighting with no taper, to trace the small-scale disk structure and (ii) natural weighting with a  $200\text{ k}\lambda$  Gaussian taper applied to long baselines, to bring out the disk emission on larger spatial scales. RMS noise levels for the resulting images as well as restoring beam sizes and position angles can be found in Table 1.3. Because the **CASA** task `tclean` preserves pointing center offsets when converting several visibility datasets into an image, it was necessary to combine the data into a single file before cleaning

**Table 1.3:** Imaging Parameters for AU Mic

Weighting Scheme	Beam Size (")	Beam PA (°)	RMS Noise ( $\mu$ Jy)
Natural (no taper)	blank	blank	blank
Natural (200 k $\lambda$ )	blank	blank	blank

in order to account for the offset in phase center between datasets. This was done using the task `concat`, which combines datasets with pointing centers aligned so long as their pointing centers do not differ by a value greater than the parameter `dirtytol`).

# Chapter 2

## Results

Figure **not here yet** shows the combined dust continuum emission from all three observations at 1.3 mm; chromospheric emission from the M star is visible as a point source at the center of the image. We report the integrated flux over regions of the disk where the flux density is in excess of three times the rms noise to be  $4972.8 \pm 14.8 \mu\text{Jy}$ ; considering that we derive an average stellar flux of **not here yet** (see Section 3), we estimate the total disk flux to be **not here yet**.

The radial structure of the disk is traced in Figure 2.1. AU Mic’s disk is resolved across  $\sim 13$  beams along the major axis, and is marginally resolved perpendicular to the major axis.  $3\sigma$  emission extends to a distance of **not here yet** on the NW side, and **not here yet** on the SE side. This discrepancy can also be seen in the upper pane of Figure 2.1.

A comparison of the brightest pixel on each side of the disk can be found in Table 2.1. We find the SE lobe to be slightly brighter than the NW side, in contrast with

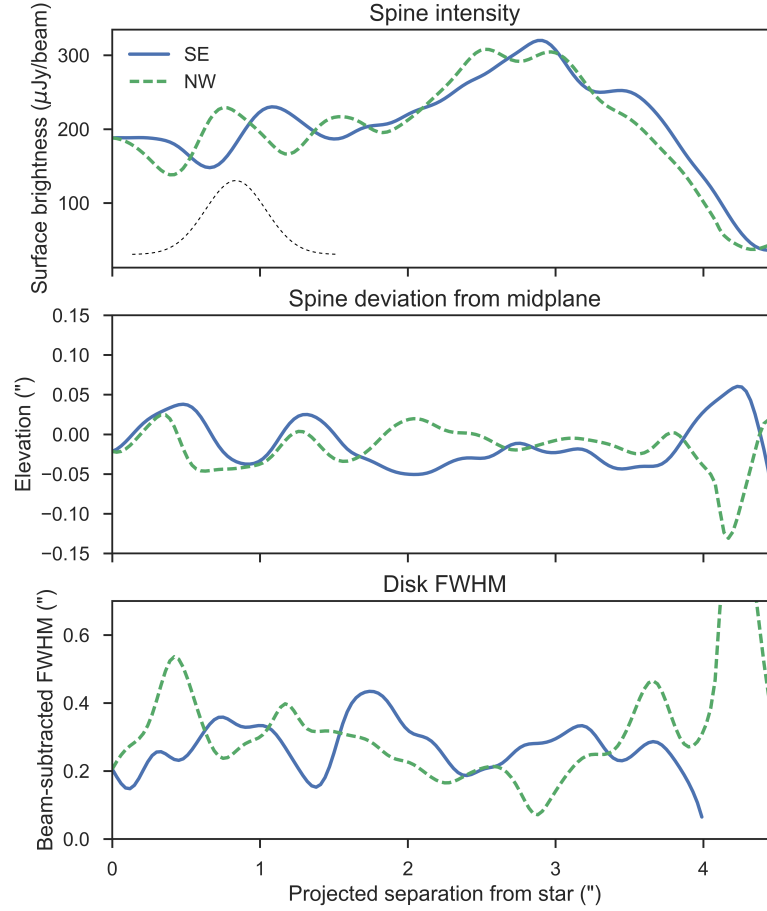


**Figure 2.1:** Image-domain analysis of AU Mic’s radial structure. At each radial location along the disk midplane, a 1-D Gaussian was fit to the vertical surface brightness profile at that location. From top to bottom, the three plots show the amplitude, centroid and width of the Gaussian fit as a function of angular separation from the star. The Gaussian traced by the dotted line in the upper pane shows the width of the synthesized beam in the radial direction. In the bottom pane, the broadening effects of the synthesized beam in the vertical direction have been removed; the fact that the image-domain vertical height of the disk is in excess of the beam contribution implies that our data spatially resolve the vertical structure of the disk.

**Table 2.1:** Comparison of the peak pixels of each ansa.

Side	Flux Density ( $\mu\text{Jy}/\text{Beam}$ )	Separation (au)	PA ( $^\circ$ )
NW	$329.2 \pm 14.8$	24.8	128.30
SE	$344.1 \pm 14.8$	29.0	128.69

MacGregor et al. (2013)’s observations which indicate the NW side to be slightly brighter. However, neither detection is significant and it is likely that the discrepancies result from fluctuations due to the RMS noise and that the dust surface brightness distribution is in fact symmetric. The disk exhibits a surface brightness profile that increases with radius, peaking at  $\sim 30$  au. As such the peak in the millimeter grain surface brightness lies interior to visible/infrared radial surface brightness peak at  $\sim 35$  au to 43 au, which has been theorized to designate a planetesimal ‘birth ring’ (Augereau & Beust 2006; Strubbe & Chiang 2006; Krist et al. 2004). Additionally, the discrepancies in PA between the two peaks do not attain significance and so we are not able to detect the PA offset described by Boccaletti et al. (2015).

# Chapter 3

## Analysis

To more rigorously analyze geometric structure of the disk and the emissive properties of the constituent dust, we model the ALMA observations directly in the visibility domain. First, a model sky image is created by a ray-tracing code from a 2-D density and temperature grid. The spatial resolution of the model image is 0.3 au per pixel, i.e. 10% of the spatial scale sampled by the longest baseline in the data. The model image is then sampled at the same spatial frequencies as the ALMA data and Fourier transformed into the visibility domain with the `MIRIAD` task `uvmodel`; this allows the model to be compared directly to the interferometric data, for which the uncertainties are better understood. A  $\chi^2$  metric is used to assess the quality of the fit.

### 3.1 Modeling Formalism

We assume the disk to be optically thin and devoid of significant levels of dust.



**Table 3.1:** MCMC

Parameter	A Run		Another Run	
	Median	Best Fit	Median	Best Fit
log Disk Mass ( $M_{\odot}$ )				
SB Law				
Scale Factor				
$r_{in}$ (au)				
$r_{out}$ (au)				
$i$ ( $^{\circ}$ )				
PA ( $^{\circ}$ )				
March $F_*$ ( $\mu\text{Jy}$ )				
August $F_*$ ( $\mu\text{Jy}$ )				
June $F_*$ ( $\mu\text{Jy}$ )				
lnprob				

- Evan talks about model here?

## 3.2 MCMC Fitting

We explore the parameter space of the model using a Markov Chain Monte Carlo (MCMC) routine. Specifically, we use the affine-invariant formulation described by Goodman & Weare (2010) and implemented in Python as `emcee` (Foreman-Mackey et al. 2013). MCMC methods sample the full breadth of the parameter space associated with a specific model, allowing the posterior probability function of each parameter to be estimated. As such, the process not only identifies regions of high probability in parameter space, but uncertainties and degeneracies between parameters can be determined by examining the correlations the posteriors of each parameter.

# Bibliography

Augereau, J.-C., & Beust, H. 2006, *A&A*, 455, 987

Boccaletti, A., Thalmann, C., Lagrange, A.-M., et al. 2015, *Nature*, 526, 230

Foreman-Mackey, D., Hogg, D. W., Lang, D., & Goodman, J. 2013, *PASP*, 125, 306

Goodman, J., & Weare, J. 2010, *Communications in Applied Mathematics and Computational Science*, Vol. 5, No. 1, p. 65-80, 2010, 5, 65

Krist, J. E., Ardila, D. R., Golimowski, D. A., et al. 2004, *ArXiv Astrophysics e-prints*, astro-ph/0410466

MacGregor, M. A., Wilner, D. J., Rosenfeld, K. A., et al. 2013, *ApJL*, 762, L21

Strubbe, L. E., & Chiang, E. I. 2006, *ApJ*, 648, 652